Spectral and particle dispersion properties of steady two-dimensional multiscale flows

M. Priego[a] and J. C. Vassilicos
Department of Aeronautics, Imperial College London, London SW7 2AZ, United Kingdom
and Institute for Mathematical Sciences, Imperial College London, London SW7 2PG, United Kingdom

(Received 9 January 2009; accepted 7 September 2009; published online 6 October 2009)

The spectral and particle dispersion characteristics of steady multiscale laminar thin-layer flows are investigated through numerical simulations of a two-dimensional layer-averaged model. The model assumes a semiparabolic velocity profile and is solved using a semi-Lagrangian spline method. The main features of the flows are turbulentlike and consistent with previous experimental studies. The Eulerian wavenumber spectra and the Lagrangian frequency spectra oscillate around power laws that reflect the self-similarity of the forcing. In the weak forcing regime, the exponents of these power laws can be related to the multiscale geometry and the intensity scaling of the forcing. The Lagrangian spectra also show low-frequency plateaus, which arise from the slow motions far away from the applied forces. The absolute dispersion of tracer particles in these steady planar flows presents a ballistic stage followed by a diffusive regime, which results from the decorrelated motions of particles lying on streamlines of different periods. Relative dispersion shows an additional intermediate stage consisting of several separation bursts, which originate from the intense strain regions imposed by the different forcing scales. While these bursts can cause locally superquadratic mean square separation, the trapping by steady recirculation regions rules out an intermediate relative dispersion power law regardless of the number of scales in the flow.
 [doi:10.1063/1.3241994]

I. INTRODUCTION

One of the outstanding features of turbulent flows is the presence of a wide range of length and time scales. The geometrical picture of multiscale motion underlies Richardson's idea of a continuous eddy cascade as well as Kolmogorov's 1941 theory,[1] which yields predictions for the turbulent energy spectrum and structure functions in the form of power laws. However, the relations between the spatiotemporal structure of turbulent flows and their prominent statistical characteristics are not yet fully understood. Two major difficulties in this direction are finding adequate geometrical descriptions of turbulent flows and establishing connections between Eulerian and Lagrangian statistics. Nevertheless, there has already been some success in applying geometrical statistics to the study of fundamental problems in turbulence. For instance, Constantin and Procaccia connected the fractal dimensions of the graphs of the hydrodynamic fields to the scaling exponents of their structure functions.[2] More recently, Davila and Vassilicos found a relation between Richardson's pair-separation exponent and the fractal dimension of the set of straining stagnation points.[3] This relation was later explained by Goto and Vassilicos,[4] who developed a pair-dispersion model based on sudden separations within a persistent, self-similar flow field.

The above connections between the multiscale structure of turbulent flows and some of their notable characteristics have already been validated in kinematic and direct numerical simulations.[3,4] On the experimental side, some of the theories have been tested on the electromagnetically forced thin-layer flows of Rossi *et al.*[5–7] Their experimental setup allows for fully controlled generation of quasi-two-dimensional multiscale flow topologies through fractal forcing arrangements. The resulting steady laminar flows, which may be regarded as kinematic, have proved similar to turbulent flows in several ways. First, their energy spectra fluctuate around power laws over the range of wavenumbers corresponding to the multiple forcing scales. These power laws have been related to the sets of multiscale stagnation points.[5] Second, particle pairs carried by these flows initially separate ballistically, then algebraically, and finally diffusively. The presence of an intermediate algebraic regime has also been explained in terms of the multiscale stagnation point structure of the flows.[5,6] Lastly, the Lagrangian frequency spectra of the flows show low-frequency plateaus followed by approximate power laws. In a first attempt toward understanding these power laws, their exponents have been connected to the algebraic pair-separation exponents and the power laws of the Eulerian wavenumber spectra.[7]

The turbulentlike features of multiscale laminar flows might as well be studied through numerical simulations of analogous thin-layer flows with fractal forcing. The numerical approach facilitates parametric studies and the testing of alternative forcing configurations. Because thin-layer flows tend to be quasi-two-dimensional when the applied forces are horizontal and small, they have traditionally been simulated using reduced, two-dimensional models.[8–10] When the applied forces are large or vertical forcing is significant, three-dimensional numerical simulations become necessary for capturing the complexities of the flow.[11,12] Since the fluid

[a]Electronic mail: martin.priego@imperial.ac.uk.

TABLE I. Parameters of the laboratory multiscale flows.

R	Geometric scaling factor	4
B_0	Remanent magnetic field	0.68 T
I	Electric current	0.04–1 A
ρ	Brine density	1103 kg m^{-3}
ν	Brine kinematic viscosity	1.326×10^{-6} m^2 s^{-1}
σ	Brine electrical conductivity	16.6 S m^{-1}
l_b	Brine layer side length	1700 mm
h_b	Brine layer thickness	5 mm
l_0	Large magnet side length	160 mm
h_0	Large magnet height	60 mm
d_0	Large magnet distance to brine	72.5 mm
l_1	Medium magnet side length	40 mm
h_1	Medium magnet height	40 mm
d_1	Medium magnet distance to brine	33.7 mm
l_2	Small magnet side length	10 mm
h_2	Small magnet height	10 mm
d_2	Small magnet distance to brine	8.5 mm

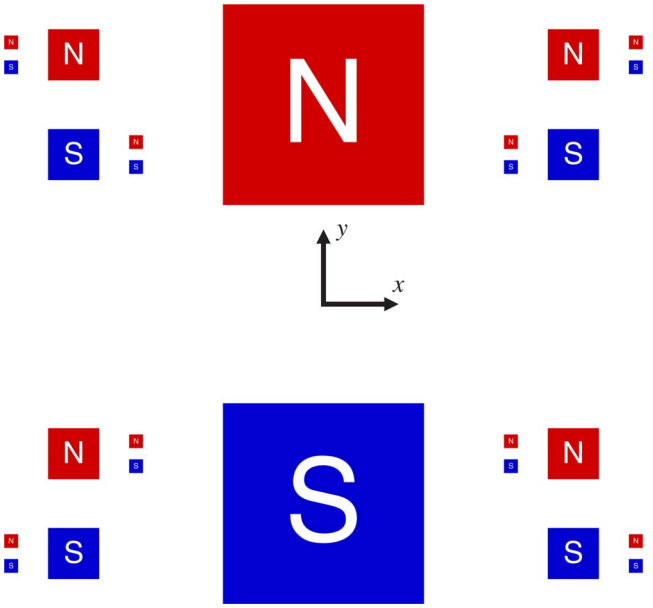

FIG. 1. (Color online) Forcing setup of the laboratory multiscale flows. The electric current flows uniformly from left to right. The magnetic field points out of the paper above north-up magnets and into the paper above south-up magnets.

responds approximately linearly to small forces, the weak forcing regime is actually most convenient for understanding the scaling properties of multiscale planar laminar flows.

In this contribution, we investigate the characteristics of steady multiscale laminar flows through numerical simulations of a layer-averaged two-dimensional model. The computations are carried out using a semi-Lagrangian spline code. After testing the model and numerical method, we examine the steady flows obtained for several forcing configurations. We extend the experimental setups by allowing for different types of self-similarity as well as for scaling of the forcing intensity. The Eulerian wavenumber spectra exhibit power laws, whose exponents we relate to the geometry and scaling of the forcing using similarity arguments. The Lagrangian frequency spectra show low-frequency plateaus followed by power laws, which we also connect to the self-similarity of the forcing. Particles released in the simulated flows disperse from their initial positions first ballistically and then diffusively. In the case of particle pairs, we corroborate the existence of an intermediate stage characterized by several separation bursts. After inspecting both the multiscale and single-scale cases, we lastly associate the bursts with the intense strain regions created by the different forcing scales. The attained understanding of the properties of steady multiscale flows will be useful for a follow-up study of the time-dependent case, where connections between Eulerian and Lagrangian statistics and related spatiotemporal features will be explored.

II. MULTISCALE THIN-LAYER FLOWS

A. Experimental and theoretical setups

In the experiment of Rossi *et al.*,[5] a thin horizontal layer of brine is forced by the combined effect of a uniform horizontal electric current and a multiscale vertical magnetic field created by a multiscale arrangement of magnets placed below the tank. The parameters of the experimental setup are summarized in Table I.

The geometry of the forcing, depicted in Fig. 1, can be described by means of iterative relations for the horizontal side lengths l_m of the magnets and the coordinates (x_m, y_m) of the centers of the oppositely oriented magnet pairs. The magnets in each pair are separated by a distance equal to their side length. The experimental setup consists of three scales: $m=0$, 1, and 2. The relations between scales m and $m+1$ take the form

$$l_{m+1} = l_m/R, \tag{1a}$$

$$x_{m+1} = x_m \pm (1+R^{-1})l_m, \tag{1b}$$

$$y_{m+1} = y_m \pm l_m, \tag{1c}$$

where R is the geometric scaling factor. In the experimental configuration, the plus-minus signs in the last two equations coincide for pairs lying in the first or third quadrants and are opposite otherwise. In our investigations, we consider the alternative combinations of the plus-minus signs that lead to the four self-similar patterns shown in Fig. 2. We denote these theoretical cases by $C=1$, 2, 3, and 4, in correspondence with the number of scaled copies of each magnet of a given scale introduced in the subsequent scale.

In the experiment, the heights h_m of the magnets do not scale with l_m and the vertical distances d_m from the centers of the magnets to the middle of the brine are adjusted in order to obtain similar forcing profiles across scales. For greater self-similarity, in our theoretical cases we set h_m and d_m equal to the side length l_m.

Finally, in the experiment all magnets have the same remanent field B_0. In contrast, we allow for scaling of the remanent field by introducing an intensity factor Q and the iterative relation

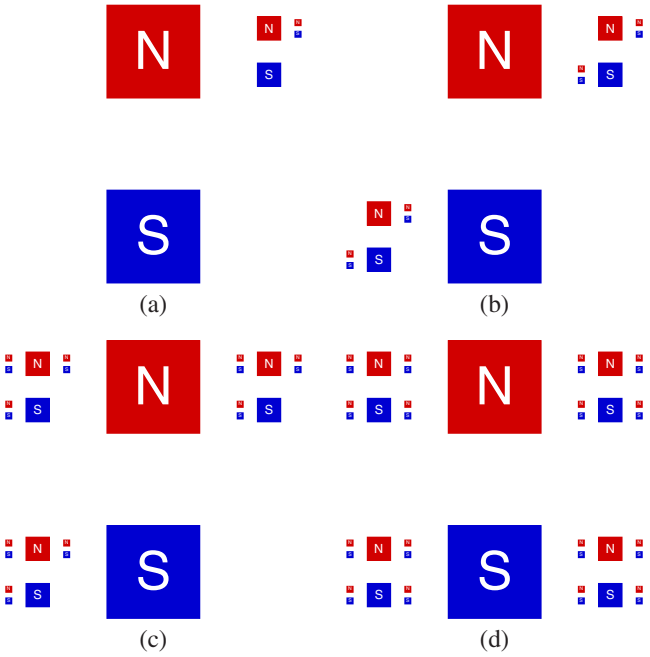

FIG. 2. (Color online) Forcing setups of the theoretical multiscale flows with $R=4$ and (a) $C=1$, (b) $C=2$, (c) $C=3$, and (d) $C=4$.

$$B_{m+1} = B_m/Q. \tag{2}$$

This scaling factor enhances the tuning of the properties of the multiscale flows. In fact, it theoretically enables the simultaneous adjustment of the Eulerian wavenumber spectrum and the Lagrangian frequency spectrum.

B. Governing equations

The movement of a conducting fluid in the presence of an electromagnetic field is governed by the equations of magnetohydrodynamics (see, e.g., Ref. 13). These consist of the Navier–Stokes equations and the low-frequency Maxwell equations coupled through the Lorentz force and Ohm's law. However, in the experiment referenced here the dynamics are greatly simplified because the fluid has negligible influence on the imposed electric and magnetic fields. Assuming the fluid to be incompressible and Newtonian, the governing equations reduce to

$$\frac{\partial u_\alpha}{\partial t} + u_\beta \frac{\partial u_\alpha}{\partial x_\beta} = -\frac{1}{\rho}\frac{\partial p}{\partial x_\alpha} + \nu \frac{\partial^2 u_\alpha}{\partial x_\beta \partial x_\beta} + f_\alpha + g_\alpha, \tag{3a}$$

$$\frac{\partial u_\alpha}{\partial x_\alpha} = 0, \tag{3b}$$

$$\rho f_\alpha = \varepsilon_{\alpha\beta\gamma} J_\beta B_\gamma, \tag{3c}$$

where Greek subscripts refer to the three Cartesian components and summation over repeated indices applies. The velocity and pressure fields are denoted by u_α and p, while ρ and ν are the density and kinematic viscosity of the fluid. The hydrodynamic fields are subject to no-slip boundary conditions at the bottom wall, $x_3=0$, and free-surface boundary conditions at the liquid-air interface, $x_3=h(x_1,x_2)$. The two rightmost terms in the momentum equation (3a) represent the actions of the Lorentz force ρf_α and the gravitational force ρg_α. In Eq. (3c) for the former, B_α is the magnetic field, J_α is the electric current density, and $\varepsilon_{\alpha\beta\gamma}$ is the totally antisymmetric tensor. Because the current induced by the flow is negligible in the experiment, the current is that resulting from the imposed electrostatic field. Likewise, the magnetic field is that due to the permanent magnets, the contribution of the electric currents being negligible.

The shallowness of the fluid layer relative to the horizontal length scales leads to further simplification of the dynamics of the laboratory flows. When the fluid layer is very thin and the forcing is weak, the flow becomes approximately two dimensional and represents a balance between the incompressible component of the forcing and the viscous friction arising from the bottom wall. Hence, the length scales present in the flow are roughly those of the forcing.

C. Asymptotic thin-layer flow

We now describe the asymptotic thin-layer regime, for it underlies the two-dimensional model introduced in Sec. III. Derivations for slightly different setups can be found in Refs. 14 and 15, while a more rigorous analysis has been carried out by Nazarov.[16] For simplicity, we consider the forcing to depend only on the horizontal coordinates and neglect its vertical component, which is very small in the experiment.

Let F and U be typical values for the intensity of the forcing and the flow speed and let h_b and L represent the mean thickness of the fluid layer and a horizontal length scale. The ratio of these two lengths defines the small parameter $\epsilon=h_b/L$. The natural scaling of the coordinates and variables is given by

$$\frac{x_i}{L} \to x_i, \quad \frac{x_3}{\epsilon L} \to x_3, \quad \frac{Ut}{L} \to t, \quad \frac{f_i}{F} \to f_i,$$
$$\frac{u_i}{U} \to u_i, \quad \frac{u_3}{\epsilon U} \to u_3, \quad \frac{h}{\epsilon L} \to h, \quad \frac{p}{\rho LF} \to p. \tag{4}$$

Here and in what follows, Latin subscripts refer to the two horizontal components (1 and 2) and Greek indices still refer to all three Cartesian components. The incompressibility equation (3b) is not altered by the above normalization, whereas the momentum equation (3a) becomes

$$\epsilon^2 \,\mathrm{Re}\left(\frac{\partial u_i}{\partial t} + u_\alpha \frac{\partial u_i}{\partial x_\alpha}\right) = -\,\mathrm{Ha}^2 \frac{\partial p}{\partial x_i} + \epsilon^2 \frac{\partial^2 u_i}{\partial x_j \partial x_j} + \frac{\partial^2 u_i}{\partial x_3^2} + \mathrm{Ha}^2 f_i, \tag{5a}$$

$$\epsilon^4 \,\mathrm{Re}\left(\frac{\partial u_3}{\partial t} + u_\alpha \frac{\partial u_3}{\partial x_\alpha}\right) = -\,\mathrm{Ha}^2 \frac{\partial p}{\partial x_3} + \epsilon^4 \frac{\partial^2 u_3}{\partial x_j \partial x_j} + \epsilon^2 \frac{\partial^2 u_3}{\partial x_3^2} - \frac{\epsilon^2 \,\mathrm{Re}}{\mathrm{Fr}^2}. \tag{5b}$$

We define the Reynolds number $\mathrm{Re}=UL/\nu$ as the ratio of inertial forces to viscous horizontal forces and assume that it is moderate in the sense that $\epsilon^2\,\mathrm{Re} \ll 1$. The Hartmann number squared $\mathrm{Ha}^2=F\epsilon^2L^2/\nu U$ represents the ratio of forcing to viscous vertical forces and is thus of order 1 in the thin-layer

limit. The Froude number squared $\mathrm{Fr}^2=U^2/g\epsilon L$, which compares inertial to gravitational forces, is assumed to be very small. In fact, to keep the perturbations of the free surface small, we assume that the forcing is much weaker than gravity in the sense that $F/\epsilon g=\mathrm{Ha}^2\,\mathrm{Fr}^2/\epsilon^2\,\mathrm{Re}\ll 1$.

The asymptotic, thin-layer solution of Eq. (4) subject to incompressibility and the aforementioned boundary conditions can be obtained by elementary means. To lowest order in ϵ, the velocities, the pressure, and the evolution of the free surface are given by

$$u_i=-\frac{\mathrm{Ha}^2}{2}\left(\frac{\partial p}{\partial x_i}-f_i\right)x_3(2h-x_3), \tag{6a}$$

$$u_3=\frac{\mathrm{Ha}^2}{6}\frac{\partial}{\partial x_i}\left[\left(\frac{\partial p}{\partial x_i}-f_i\right)x_3^2(3h-x_3)\right], \tag{6b}$$

$$p=\frac{\epsilon^2\,\mathrm{Re}}{\mathrm{Ha}^2\,\mathrm{Fr}^2}\left(h-x_3-\frac{1}{\mathrm{Bo}}\frac{\partial^2 h}{\partial x_i\,\partial x_i}\right), \tag{6c}$$

$$\frac{\partial h}{\partial t}=\frac{\mathrm{Ha}^2}{3}\frac{\partial}{\partial x_i}\left[h^3\left(\frac{\partial p}{\partial x_i}-f_i\right)\right]. \tag{6d}$$

Here, the Bond number $\mathrm{Bo}=\rho g L^2/\gamma$ compares gravity to surface tension forces, with γ being the surface tension coefficient. When $\mathrm{Bo}\gg 1$ and $\mathrm{Ha}^2\,\mathrm{Fr}^2/\epsilon^2\,\mathrm{Re}\ll 1$, the pressure is hydrostatic and the free surface reacts rapidly, yet slightly, to cancel the compressible part of the forcing. The resulting steady flow is horizontal and varies along the vertical coordinate according to the semiparabolic profile (6a). This type of parallel, profiled flow is the basis of the reduced two-dimensional model.

III. NUMERICAL SIMULATION

A. Two-dimensional layer-averaged model

The results of Sec. II are valid provided the fluid layer is very thin compared to length scales of the flow ($\epsilon\ll 1$), the Reynolds number is moderate ($\epsilon^2\,\mathrm{Re}\ll 1$), and the forcing and surface tension forces are very weak compared to the gravitational force ($\mathrm{Ha}^2\,\mathrm{Fr}^2/\epsilon^2\,\mathrm{Re}\ll 1$ and $\mathrm{Bo}\gg 1$). Since the last two conditions are invariably met in the experiment, the fluctuations of the free surface are very small in the laboratory flows. However, the first two conditions are generally not satisfied, especially at the smaller scales (i.e., for small L). As a result, inertial and horizontal viscous effects neglected in the asymptotic analysis are likely to be present in laboratory flows. For those cases where special care might be taken to realize all the above conditions, but also for fundamental studies of multiscale planar laminar flows, an approximate two-dimensional model is very desirable. For thin film flows, such models are typically derived by prescribing the form of the horizontal velocity distribution across the fluid layer and subsequently averaging the governing equations along the vertical direction.[14,15]

In light of the asymptotic results, we assume that the horizontal velocity distributions across the layer are given by the semiparabolic profiles

$$u_i x_3(2h_b-x_3)/h_b^2, \tag{7}$$

where u_i now denote the horizontal velocities at the free surface. Given that the fluctuations of the free surface are very small, we neglect them along with the vertical velocity. Substituting the velocity profiles in the Navier–Stokes equation (3a) and averaging across the layer yields the two-dimensional model equation

$$\frac{\partial u_i}{\partial t}+\frac{4}{5}u_j\frac{\partial u_i}{\partial x_j}=-\frac{3}{2\rho}\frac{\partial p}{\partial x_i}+\nu\frac{\partial^2 u_i}{\partial x_j\,\partial x_j}+\frac{3}{2}(f_i-\beta u_i), \tag{8}$$

again subject to incompressibility. Here, $\beta=2\nu/h_b^2$ is the bottom friction coefficient and p and f_i are actually the averages of the pressure and forcing across the layer. This model is essentially the two-dimensional Navier–Stokes equations with some modified coefficients and an additional linear term representing viscous friction from the bottom wall. The model resembles other modified Navier–Stokes equations that have proved suitable for the type of flow considered here.[8–10] A possible advantage of the averaged model is that it accounts for the assumed velocity profile globally.

We numerically solve the reduced model using the semi-Lagrangian spline code described in the Appendix. The code actually solves the equivalent vorticity equation

$$\frac{\partial \omega}{\partial t}+\frac{4}{5}u_j\frac{\partial \omega}{\partial x_j}=\nu\frac{\partial^2 \omega}{\partial x_j\,\partial x_j}-\frac{3}{2}\beta\omega+\frac{3}{2}\varphi, \tag{9a}$$

$$\frac{\partial^2 \psi}{\partial x_i\,\partial x_i}=-\omega,\quad u_i=\varepsilon_{ij}\frac{\partial \psi}{\partial x_j}. \tag{9b}$$

Here, ψ is the streamfunction, $\omega=\varepsilon_{ij}\partial u_j/\partial x_i$ is the vorticity, and $\varphi=\varepsilon_{ij}\partial f_j/\partial x_i$ is the vorticity forcing. In the laboratory flows f_1 vanishes because the current is parallel to the x_1-axis, so that φ reduces to $\partial f_2/\partial x_1$. We carry out our simulations in a biperiodic domain with the same side length l_b as the experimental tank using splines of order $\kappa=7$ and $n=2048$ grid points along each direction. This resolution corresponds to about 12 collocation points along the side of the smallest magnets and therefore captures all the length scales of the flow.

B. Comparison with experiment

We test our model and numerical methods by computationally reproducing one of the experimental flows of Rossi *et al.*[5] We consider the well-documented case with electric current $I=0.3$ A and remaining parameters as specified in Table I. The layer-averaged model cannot be expected to provide accurate results for the smallest scales in this moderately forced flow, but our ultimate aim is only to understand how the fundamental characteristics of multiscale laminar flows arise. In Fig. 3, we show the results for the steady state eventually achieved in a simulation carried out with time step $\Delta t=6.667$ ms. The multiscale pattern of streamlines and the spatial distribution of velocity are in visual agreement with the laboratory measurements (see Fig. 9 in Ref. 5). The maximum speed of the simulated flow, 16.31 mm s^{-1}, is about 5% higher than the experimental value, 15.6 mm s^{-1}. We deem this agreement satisfactory for

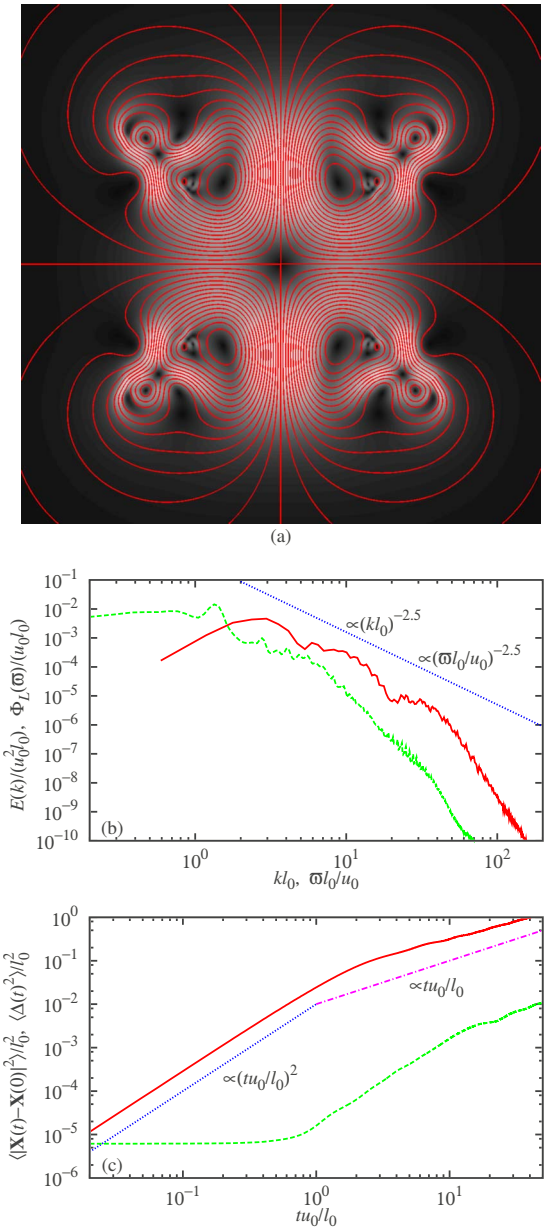

FIG. 3. (Color online) Simulation results for the experimental flow with current $I=0.3$ A: (a) velocity magnitude (bright=fast, dark=slow) and streamlines in the central square of side length $l_b/2$, (b) Eulerian wavenumber (solid line) and Lagrangian frequency (dashed line) spectra, and (c) absolute (solid line) and relative (dashed line) particle dispersions.

our purposes and ascribe the discrepancies to the three-dimensional effects disregarded in the modeling.

In Fig. 3(b), we present the Eulerian wavenumber spectrum $E(k)$ and the Lagrangian frequency spectrum $\Phi_L(\varpi)$ of the simulated flow. Both densities integrate to the specific kinetic energy of the flow,

$$\langle|\mathbf{u}|^2\rangle = 2\int_0^\infty E(k)dk = 2\int_0^\infty \Phi_L(\varpi)d\varpi, \tag{10}$$

and are made dimensionless using the side length of the largest magnets, l_0, and the large-scale velocity, $u_0=15.46$ mm s^{-1}. We define the latter as the maximum velocity in a simulation with the same parameters forced only at the largest scale. Thus, u_0 provides a measure of the large-scale velocity independent of the scaling and geometrical parameters. We obtain the Lagrangian spectrum by following 1024^2 ideal particles released as a regular grid into the steady flow. In the intermediate wavenumber and frequency ranges, both spectral density curves might be interpreted as power laws multiplied by bounded oscillatory functions. Like in the corresponding laboratory measurements (see Fig. 14 in Ref. 5 and Fig. 2 in Ref. 7), the exponents of the two power laws are not far from -2.5. The Lagrangian spectrum shows an additional low-frequency plateau, which also agrees with the experimental findings. We analyze and provide simple explanations for the spectral properties of flows of this type in Sec. IV.

In Fig. 3(c), we plot particle dispersion results based on the tracking of 1024^2 initially equilateral triangles of side length of 0.3972 mm released uniformly into the steady flow. The evolution of mean square particle displacement $\langle|\mathbf{X}(t)-\mathbf{X}(0)|^2\rangle$ is qualitatively similar to the experimental one (see Fig. 1 in Ref. 7). In both cases, an initial ballistic regime of quadratic growth is followed by a diffusive stage of linear growth, which does not saturate in the displayed time interval. However, the two results differ in scale because the experimental one only accounts for particles traversing the central flow region, where the forcing is concentrated. The evolution of mean square relative dispersion $\langle\Delta(t)^2\rangle$, calculated using the side lengths of the tracked triangles, moderately resembles that of the laboratory flow (see Fig. 5 in Ref. 6). The initial plateau conceals the quadratic growth of relative dispersion at the very outset, which can be revealed by subtracting the squared initial separation, as we do in Sec. V B. This ballistic regime is followed by an intermediate algebraic stage with exponent slightly below 2 and, lastly, by a diffusive regime. In contrast, the exponent of the intermediate stage in the experiment is approximately 2.7. We ascribe this discordance partly to the differences between the simulated and laboratory flows, but mainly to the sampling procedure used for the experimental results, which only accounts for particle pairs crossing the central region. We defer the detailed study of particle dispersion characteristics to Sec. V.

IV. SPECTRAL CHARACTERISTICS

We now study the spectral characteristics of steady two-dimensional multiscale flows in the theoretical settings described in Sec. II A. These forcing configurations have clearer self-similarity than the experimental one, and thus their scaling properties are more easily obtained. We carry out our simulations with electric current $I=0.01$ A and time step $\Delta t=0.2$ s. With such weak forcing, the steady flows approximately result from the balance between the incompressible component of the forcing and the viscous friction arising from the bottom wall. We examine three different combinations of geometric scaling factor R and intensity scaling factor Q: $R=4$ and $Q=1$, $R=\sqrt{8}$ and $Q=1$, and $R=4$ and $Q=\sqrt{2}$. For each of these combinations, we consider the four self-similar magnet arrangements denoted by the multipliers $C=1$, 2, 3, and 4 (see Fig. 2). The resulting

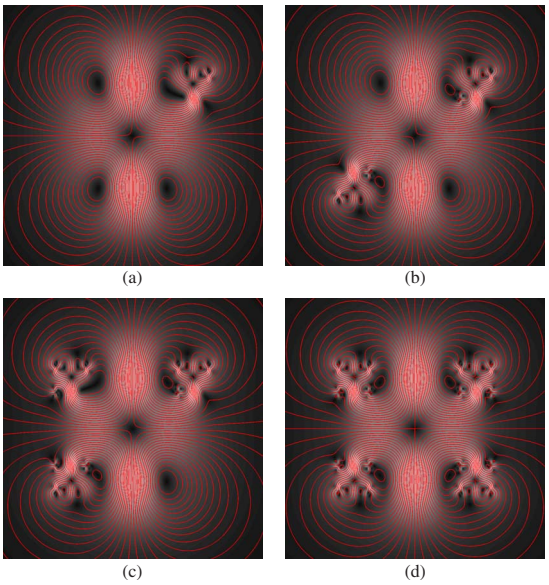

FIG. 4. (Color online) Velocity magnitude (bright=fast, dark=slow) and streamlines of the theoretical multiscale flows in the central square of side length of $l_b/2$. The scaling and geometrical parameters are $R=4$, $Q=1$, and (a) $C=1$, (b) $C=2$, (c) $C=3$, and (d) $C=4$.

flow fields for the cases with $R=4$ and $Q=1$ are shown in Fig. 4. The streamline patterns clearly expose the multiscale topology of the flows, while the velocity magnitude fields reflect to good extent the self-similarity of the forcing. Indeed, in the weak forcing case, the velocity field is roughly a superposition of scaled translations of the velocity field created by a single pair of magnets. This trivial observation is key to our understanding of the spectral properties of these flows.

A. Eulerian wavenumber spectra

Given the approximate proportionality between the solenoidal component of the forcing and the fluid velocity, the features of their spectra should be the same in the weak forcing regime. This must actually be the case whenever interscale energy transfers and horizontal viscous dissipation are relatively small.

Likewise to the energy spectrum, we define the spectral density of the forcing $F(k)$ so that it integrates to half of the mean square specific forcing,

$$\langle |\mathbf{f}|^2 \rangle = 2 \int_0^\infty F(k) dk. \tag{11}$$

In Fig. 5(a), we present the spectra of the different forcings, normalized using the side length of the largest magnets, l_0, and the large-scale forcing, $f_0=99.90\ \mu\text{m s}^{-2}$, defined as the maximum specific force caused by the largest magnet pair. The three different forcing scales appear as three humps in the spectral density curves. In the intermediate region, each curve may be fitted by a power law $(kl_0)^{-p}$ multiplied by a bounded oscillatory function. The exponent p must then be related to the similarities of the forcing.

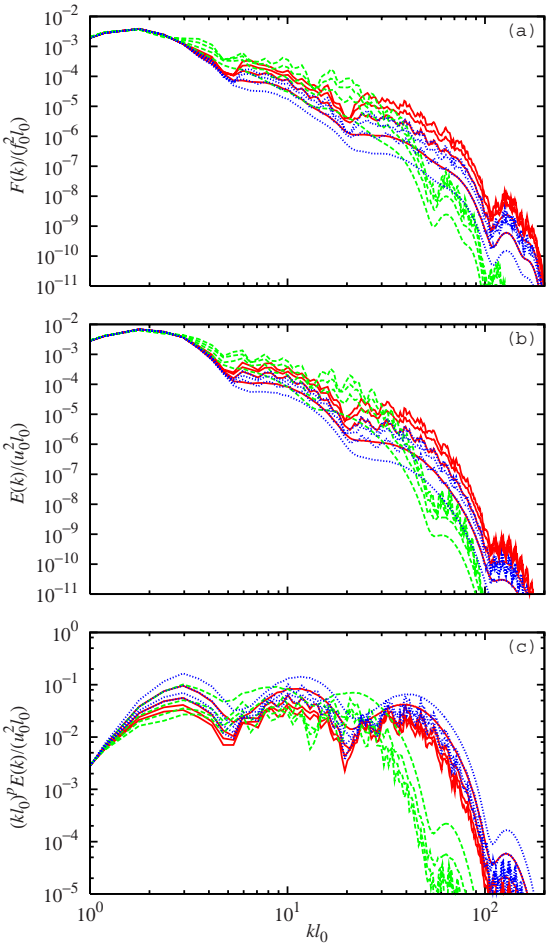

FIG. 5. (Color online) (a) Forcing wavenumber spectra and (b) uncompensated and (c) compensated Eulerian wavenumber spectra of the theoretical multiscale flows. The compensating power is $p=3-\log(C/Q^2)/\log R$. The scaling and geometrical parameters are $R=4$ and $Q=1$ (solid line), $R=\sqrt{8}$ and $Q=1$ (dashed line), and $R=4$ and $Q=\sqrt{2}$ (dotted line) and $C=1$, 2, 3, and 4 from bottom to top in (a) and (b).

In order to determine the scaling of the forcing spectrum, we first notice that the force caused by the magnets of scale l_m mainly contributes to wavenumbers close to l_m^{-1}, say, between l_m^{-1} and l_{m+1}^{-1}. Because the magnets are well separated, their contributions to the mean square forcing are nearly additive. Consider now the difference in contribution between the magnets of scale l_m and those of scale $l_{m+1}=l_m/R$. The effective area of influence of the larger scale forcing is R^2/C times that of the smaller, while the local force intensity is larger by a factor Q at the larger scale. As a result, the contribution of the larger scale to the mean square forcing is Q^2R^2/C times that of the smaller scale. Assuming that the contributions from the different forcing scales to the spectrum are additive, we obtain that the spectral density between scales l_m^{-1} and l_{m+1}^{-1} must be greater than that between l_{m+1}^{-1} and l_{m+2}^{-1} by a factor of Q^2R^3/C. Consequently, within the intermediate, self-similar wavenumber range, the scaling of forcing spectrum is given by

$$F(k) \propto f_0^2 l_0 (kl_0)^{-p} \quad \text{with} \quad p = 3 - \frac{\log C/Q^2}{\log R}, \tag{12}$$

where we include the large-scale characteristic values for dimensional consistency. For accuracy, the above power law

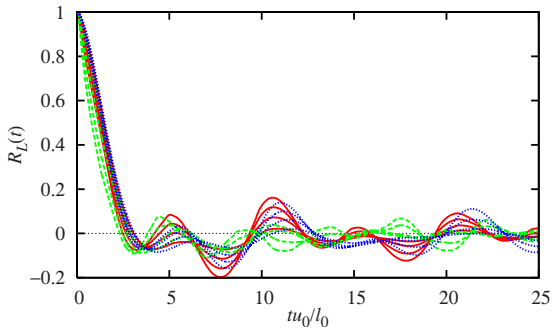

FIG. 6. (Color online) Lagrangian velocity correlation of the theoretical multiscale flows. The scaling and geometrical parameters are $R=4$ and $Q=1$ (solid line), $R=\sqrt{8}$ and $Q=1$ (dashed line), and $R=4$ and $Q=\sqrt{2}$ (dotted line) and $C=1$, 2, 3, and 4 from smaller to greater fluctuations.

should be multiplied by an oscillatory function of kl_0 with fixed lower and upper bounds.

By the argument above, we would expect the Eulerian wavenumber spectrum $E(k)$ to follow the same scaling as the forcing spectrum, that is,

$$E(k) \propto u_0^2 l_0 (kl_0)^{-p} \quad \text{with} \quad p = 3 - \frac{\log C/Q^2}{\log R}. \tag{13}$$

Here, u_0 is again the characteristic velocity of the largest scale, which for these theoretical flows with $I=0.01$ A is 0.4123 mm s^{-1}. Formula (13) corrects and generalizes the relation $p=\text{const}-1/\log R$ put forward by Hascoët *et al.*[10] In Fig. 5(b), we plot the Eulerian wavenumber spectra of the flows. The energy curves closely resemble those of the forcing except at the highest wavenumbers, where the energy decays more rapidly. This lack of proportionality between the energy and forcing spectra at the small scales is due to the higher influence of inertial and viscous horizontal forces, as seen in Sec. II C. The validity of the proposed scaling in the intermediate wavenumber range is confirmed in Fig. 5(c), which shows the energy spectra compensated by $(kl_0)^p$ with p given by Eq. (13). Indeed, the compensated curves oscillate about horizontal lines except at the smallest scales.

The observed scaling of the Eulerian wavenumber spectrum is thus an elementary consequence of the self-similarity of the forcing and the approximate linearity between weak forcing and fluid velocity. Based on this understanding, we interpret the -2.5 exponent measured in the moderately forced laboratory flows in the following way.[5] The experimental flows have scaling parameters $R=4$ and $Q=1$, while the multiplier C takes the values of 4 from the large to the medium scale and 2 from the medium to the small scale. According to the scaling (13), the corresponding exponents would be -2 and -2.5. Because of horizontal viscous effects and stronger interscale energy transfers at moderate forcing, the exponents seen in Fig. 3(b) are slightly above and below -2.5, roughly yielding a -2.5 spectrum across the intermediate wavenumber range.

B. Lagrangian frequency spectra

We analyze the Lagrangian frequency spectrum using the same framework as for the wavenumber spectrum. In order to calculate the Lagrangian spectra, we track 1024^2 particles released as a regular grid into the steady flows. As intermediate products, we obtain unbiased estimates for the Lagrangian velocity correlations,

$$R_L(t) = \langle \mathbf{u}_L(0) \cdot \mathbf{u}_L(t) \rangle / \langle |\mathbf{u}|^2 \rangle, \tag{14}$$

where $\mathbf{u}_L(t)$ denotes the Lagrangian velocity of a fluid element at time t. In Fig. 6, we show the Lagrangian correlation estimates for the different flows. The general features of these functions are similar to the experimental ones reported in Ref. 7. The correlation curves first cross zero at $t \sim 2l_0/u_0$ and oscillate thereafter while slowly decaying. The Lagrangian correlation time, defined as the semi-infinite integral of $R_L(t)$, thus takes values of the order of the characteristic time l_0/u_0 of the large scale. However, the mechanism leading to the long-time Lagrangian decorrelation is rather peculiar because almost every particle trajectory is periodic in these steady planar flows. Hence, the asymptotic decay of the correlation function is possible because the particle ensemble spans infinitely many streamlines with incommensurate periods. A study of the decorrelation rate and its relation to the shearing action of the multiscale flows is, however, beyond the scope of this work.

We obtain the Lagrangian frequency spectra $\Phi_L(\varpi)$ by Fourier transforming the Lagrangian covariances. We actually premultiply these covariance estimates by a cubic B-spline window to mitigate the spectral corruption caused by their finiteness in time.[17] We present the resulting Lagrangian frequency spectra in Fig. 7(a). Like those of the laboratory flows,[7] they consist of low-frequency plateaus followed by approximate power laws and, ultimately, faster downfalls.

Once again, we attribute the intermediate power laws to the similarities of the forcing and their reflection on the velocity field. When the forcing is weak, the magnet pairs of side length l_m cause local velocities u_m of order u_0/Q^m. Since the spatial scale of variation of these steady velocities is l_m, their characteristic Lagrangian frequency must be u_m/l_m. By the same argument as for the wavenumber spectrum, the spectral density between frequencies u_m/l_m and u_{m+1}/l_{m+1} is greater than that between u_{m+1}/l_{m+1} and u_{m+2}/l_{m+2} by a factor of QR^3/C. Because the two considered frequency ranges are related by R/Q, the expected scaling of the Lagrangian spectrum is then given by

$$\Phi_L(\varpi) \propto u_0 l_0 (\varpi l_0/u_0)^{-q} \quad \text{with} \quad q = 3 - \frac{\log C/Q^4}{\log R/Q}. \tag{15}$$

We test this prediction in Fig. 7(b), where we plot the spectra compensated by $(\varpi l_0/u_0)^q$ with q given by Eq. (15). The compensated curves for $Q=1$ fluctuate around horizontal lines in the intermediate frequency range, though they slightly decay due to the greater influence of inertial and horizontal viscous forces at small scales. In contrast, in the cases with $Q=\sqrt{2}$ the compensated curves rise noticeably toward the higher frequencies. The reason for this deviation

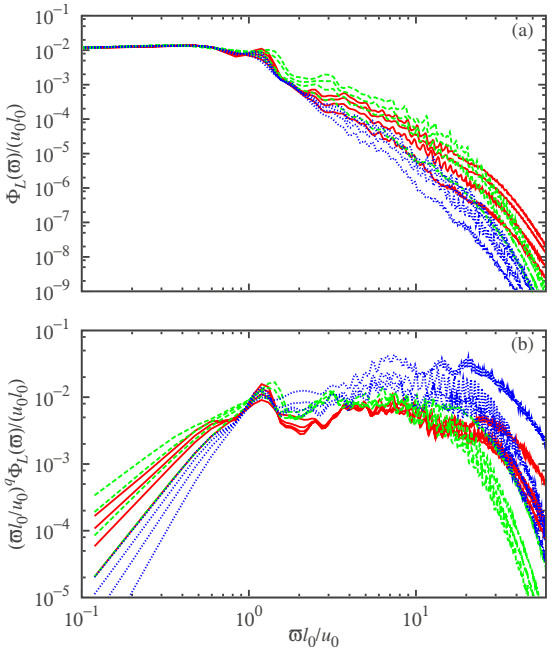

FIG. 7. (Color online) (a) Uncompensated and (b) compensated Lagrangian frequency spectra of the theoretical multiscale flows. The compensating power is $q=3-\log(C/Q^4)/\log(R/Q)$. The scaling and geometrical parameters are $R=4$ and $Q=1$ (solid line), $R=\sqrt{8}$ and $Q=1$ (dashed line), and $R=4$ and $Q=\sqrt{2}$ (dotted line) and $C=1$, 2, 3, and 4 from bottom to top in (a).

from the predicted scaling can be found by reinspecting the velocity fields presented in Fig. 4. Although $Q=1$ in those flows, the velocities above the large magnets are somewhat smaller than those above the medium and small magnets. This shows that the velocity on top of each magnet pair is actually affected by the larger magnet pairs, which can modify the local velocity and frequency scales used in the derivation of law (15). This effect is more pronounced the larger the value of Q, and thus the predicted scaling seems approximately valid for $Q=1$ but fails to work for the cases with $Q=\sqrt{2}$. However, we shall be content with this understanding of the Lagrangian spectrum and not pursue a precise relation for its scaling, as it would depend on the geometrical details of the forcing configuration.

Regardless of the validity of the Lagrangian law (15), our analysis of the Eulerian wavenumber and Lagrangian frequency spectra suggests that they follow different intermediate scaling laws when $Q\neq 1$. Theoretically, this would enable the simultaneous adjustment of the power laws of the two spectral densities. For instance, according to the scalings (13) and (15), the parameters $C=4$, $R=2$, and $Q=\sqrt[3]{2}$ would give rise to the inertial range spectra of turbulence,[18] $E(k)\propto(u_0^3/l_0)^{2/3}k^{-5/3}$ and $\Phi_L(\varpi)\propto(u_0^3/l_0)\varpi^{-2}$. However, with such a small value of R, either the self-similar range would be very small (two octaves) or the forcing configuration described by relations (1) and (2) would not be physically realizable because the magnets of different scales would overlap.

We attribute the low-frequency plateaus observed in the Lagrangian spectra to the slow flows far away from the applied forces. In the considered flows, vorticity is generated in opposite pairs above each magnet and remains confined to the central region. As a result, the flow distant from the origin can be approximated by a multipole expansion based on the vorticity moments.[19] For simplicity, we use Green's function for the Poisson equation in the plane, which is strictly not valid in our periodic domain but reveals the essential features. Thus, we approximate the streamfunction at points $\mathbf{r}$ far from the origin but not too close to the boundary by

$$2\pi\psi(\mathbf{r}) \sim -\log r \int \omega(\mathbf{x})d\mathbf{x} + \sum_i \frac{r_i}{r^2}\int x_i\omega(\mathbf{x})d\mathbf{x} - \sum_{i,j}\left(\frac{\delta_{ij}}{2r^2}-\frac{r_i r_j}{r^4}\right)\int x_i x_j\omega(\mathbf{x})d\mathbf{x} + O(r^{-3}), \tag{16}$$

where δ_{ij} is the Kronecker delta. Because the forcing configurations consist of antialigned force pairs, they are incapable of creating circulation at infinity or hydrodynamic impulse, so the two first terms in the expansion (16) vanish in the resulting flows. Hence, the far velocity fields are dominated by quadrupoles and the streamfunction decays like r^{-2}. The velocity field is then of order r^{-3} and has local length scale r. Consequently, the annulus of radii r and $r+dr$ contains energy commensurate with r^{-5} and primarily contributes to a frequency band proportional to $[r^{-4}-4r^{-5}dr, r^{-4}]$. It follows that the energy per unit frequency is roughly constant in the distant flows, leading to flat Lagrangian spectra at low frequencies.

V. PARTICLE DISPERSION CHARACTERISTICS

We now investigate the particle dispersion characteristics of the weakly forced, two-dimensional multiscale flows introduced in Sec. IV. The results are based on the tracking of 1024^2 initially equilateral triangles of side length $\Delta(0)=1.660$ mm released uniformly into the steady flows. This initial separation corresponds to twice the distance between grid points and is still much smaller than the smallest scale of the forcing and velocity fields. We numerically integrate the trajectories $\mathbf{X}(t)$ of the vertices using a second-order Runge–Kutta method and the spline representation of the velocity field. We examine the evolution of mean square particle displacement $\langle|\mathbf{X}(t)-\mathbf{X}(0)|^2\rangle$, which characterizes absolute dispersion, and that of the mean square side length of the triangles $\langle\Delta(t)^2\rangle$, which measures relative dispersion.

A. Absolute dispersion

In Fig. 8, we present the mean square displacements corresponding to the different forcing configurations, normalized using the side length of the largest magnets, l_0, and the large-scale velocity, $u_0=0.4123$ mm s^{-1}. Like in the laboratory flows, the curves show an initial ballistic stage, with $\langle|\mathbf{X}(t)-\mathbf{X}(0)|^2\rangle\propto u_0^2t^2$, followed by a diffusive stage, where $\langle|\mathbf{X}(t)-\mathbf{X}(0)|^2\rangle\propto l_0u_0t$. In all cases the transition between the two regimes takes place at times of the order of l_0/u_0, which is close to the Lagrangian correlation time (see Sec. IV B). The observed dispersion thus complies with Taylor's

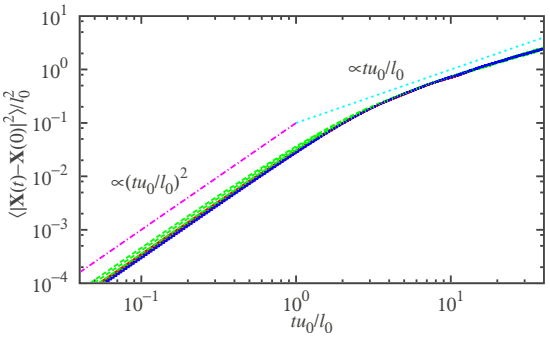

FIG. 8. (Color online) Absolute dispersion of the theoretical multiscale flows. The scaling and geometrical parameters are $R=4$ and $Q=1$ (solid line), $R=\sqrt{8}$ and $Q=1$ (dashed line), and $R=4$ and $Q=\sqrt{2}$ (dotted line) and $C=1$, 2, 3, and 4 from bottom to top.

analysis,[1] but the diffusive regime arises here from the decorrelated motions of particles lying on many different periodic streamlines.

The differences among the various absolute dispersion curves are only noticeable in the ballistic regime. For very small times, the mean square displacement is in fact proportional to the specific kinetic energy, $\langle |\mathbf{X}(t)-\mathbf{X}(0)|^2\rangle \propto \langle |\mathbf{u}|^2\rangle t^2$. A straightforward similarity argument, akin to those of Sec. IV A, shows that in these weakly forced flows the kinetic energy is connected to the scaling and geometrical parameters by

$$\langle |\mathbf{u}|^2\rangle \propto u_0^2 \sum_m C^m R^{-2m} Q^{-2m}. \tag{17}$$

This approximate relation for the kinetic energy explains the initial order of the dispersion curves in Fig. 8. In particular, the initial growth rate of absolute dispersion increases with the multiplier C and decreases with the scaling factors R and Q.

B. Relative dispersion

In Fig. 9(a), we plot the mean square dispersion of particle pairs, calculated from the side lengths of the traced triangles. As in the experimental flows, we find an initial stage of relative constancy with underlying ballistic separation as well as a final diffusive stage of approximately linear growth. However, between these two regimes it is not *a priori* clear how to fit the relative dispersion curves, whose shape actually depends on the scaling and geometrical parameters.

The quadratic growth of relative dispersion at the very beginning is evidenced by the flat initial segments in Fig. 9(b), where we plot the mean square dispersion discounted for the initial separation and compensated by $(tu_0/l_0)^{-2}$. At the outset pair-separation results from the local strain rate, though incompressibility makes the initial growth rate vanish when averaged over all possible pair orientations. Mean square dispersion is therefore quadratic in time and roughly proportional to the mean square velocity gradient, $\langle \Delta(t)^2 - \Delta(0)^2\rangle \propto \Delta(0)^2 \langle |\nabla \mathbf{u}|^2\rangle t^2$. By a similarity argument analogous to that used for the kinetic energy, the predicted scaling of the velocity gradient is

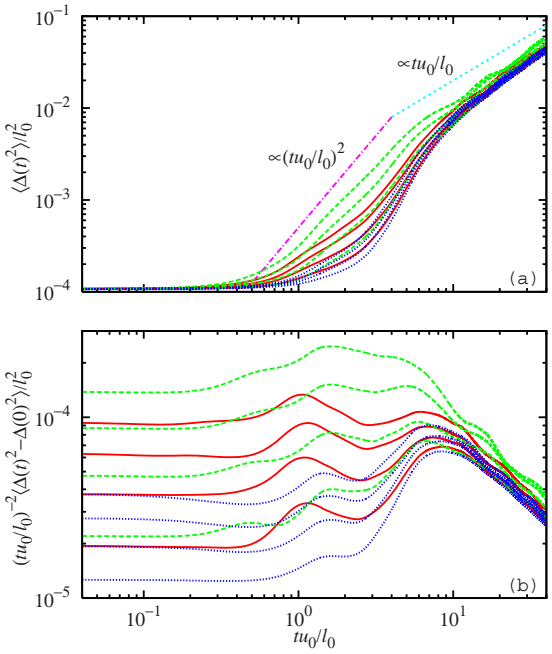

FIG. 9. (Color online) (a) Uncompensated and (b) compensated relative dispersions of the theoretical multiscale flows. The scaling and geometrical parameters are $R=4$ and $Q=1$ (solid line), $R=\sqrt{8}$ and $Q=1$ (dashed line), and $R=4$ and $Q=\sqrt{2}$ (dotted line) and $C=1$, 2, 3, and 4 from bottom to top.

$$\langle |\nabla \mathbf{u}|^2\rangle \propto (u_0/l_0)^2 \sum_m C^m Q^{-2m}. \tag{18}$$

Owing to the lack of proportionality between forcing and velocity at small scales (see Fig. 5), this relation is not strictly satisfied in these flows. Otherwise, the initial dispersion rate would be independent of the geometric scaling factor R, in discordance with the results in Fig. 9(b). Nonetheless, the above relation qualitatively explains the influence of the remaining parameters in the ballistic regime.

The compensated plot also reveals that pair dispersion has a superquadratic behavior in the intermediate stage punctuated by several bumps. In line with Rossi *et al.*,[5,6] we attribute these bumps to major dispersion contributions from the three different scales of the flow. The last, strong burst prior to the diffusive regime nearly coincides in time in all cases and is caused by the largest scale. The first, weak bump is due to the smallest scale and is only appreciable in the cases with $R=\sqrt{8}$. In support of this correspondence, the onset times of the first three bursts are approximately related by the same factor R/Q relating the characteristic time scales l_m/u_m of the flows (see Sec. IV B for u_m). As well, the size of the intermediate bumps is roughly commensurate with the multiplier C, which represents the number of medium scale magnets. However, the combined action of the different flow scales does not seem to invariably yield algebraic relative dispersion in the intermediate regime. Furthermore, it is clear from Fig. 9 that hypothetical power law fits to the midsections of the relative dispersion curves would have smaller exponent the larger C and the smaller Q. In fact, the trend suggests that all these exponents would be smaller than the intermediate log-log slope of relative dispersion in the flow forced only at the largest scale. Our explanation for this pe-

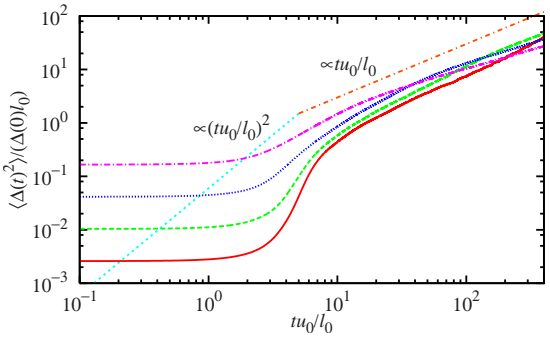

FIG. 10. (Color online) Relative dispersion of the theoretical single-scale flow for various initial separations.

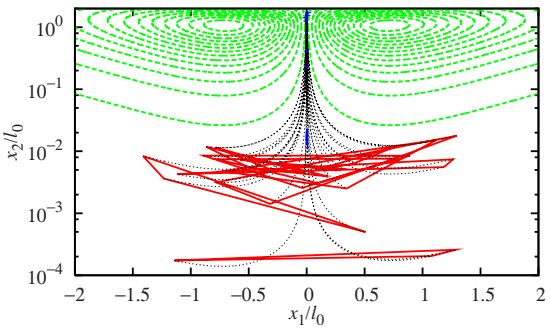

FIG. 11. (Color online) Tracer triangles (solid line) dominating relative dispersion growth at time $5l_0/u_0$ in the single-scale flow. Streamlines (dashed line) and trajectories (dotted line) are shown.

culiarity is that, in these steady two-dimensional flows, the early separations caused by the small scales are not significantly augmented by the larger scales, in marked contrast with Richardson dispersion in turbulent flows (see, e.g., Ref. 1). Because the flows are stationary, fluid elements are trapped within steady recirculation regions. For instance, individual pairs belonging to small-scale neighboring streamlines remain forever in those same streamlines, and thus they cannot reach separations comparable to the large scale.

The outset of the diffusive regime is visible in both the compensated and uncompensated plots. The final growth of mean square dispersion is slightly faster than linear, but the diffusive stage should eventually be reached and at some point saturate. Like for absolute dispersion, the diffusive regime arises from the collective divergence and convergence of particle pairs. The two particles in each typical pair separate and gather in a quasiperiodic fashion, with the basic frequencies being those of the two streamlines involved. Decorrelation across the different pairs leads to a linear relative dispersion law of the form $\langle \Delta(t)^2 \rangle \propto \Delta(0) u_0 t$. This is the only dimensionally consistent linear-in-time law that can be constructed from the large length scale l_0 and the frequency difference of two large closed streamlines separated by about $\Delta(0)$, which is of order $u_0 \Delta(0)/l_0^2$. The above diffusive law neglects the influence of the smaller scales, which should be included for accuracy. The dependence on initial separation at such advanced separation stage is again due to the steadiness of these two-dimensional flows.

We check the foregoing interpretation of relative dispersion in the multiscale flows by likewise inspecting its behavior in the flow forced only at the largest scale. In Fig. 10, we present dispersion results obtained from the long-time tracking of four groups of 256^2 triangles released uniformly into the single-scale steady flow. The initial side lengths of the triangles in each group are related to the previously used $\Delta(0) = 1.660$ mm by a power of 4. For later convenience, in Fig. 10 we normalize mean square separation using the product $\Delta(0) l_0$. As in the multiscale flows, the dispersion curves show initial plateaus with underlying quadratic growth of mean square separation. This ballistic regime is succeeded by a dispersion burst, which happens approximately at the same time in the four curves. The burst is especially noticeable when the initial separation is small, with the local growth being significantly faster than quadratic in the bottom two curves. In Fig. 11 we show the trajectories of the upper-half triangles of initial side length 1.660 mm that contribute most to the increase in mean square dispersion at time $5l_0/u_0$. While the displayed triangles are only 0.04% of the total, they account for 95% of the separation rate. In view of this figure, we attribute the burst to the triangles initially located close to the magnets and the x_2-axis. Regardless of their initial size, these triangles are coherently stretched in an exponential-like manner as they traverse the highly straining central region in time proportional to l_0/u_0. Obviously, the sustained type of exponential separation behavior found in chaotic systems is impossible in these integrable two-dimensional flows. Based on this perception, we regard the bumps in the multiscale dispersion curves as reflections of the passages through the intense strain regions corresponding to the different scales, thus occurring at times approximately proportional to l_m/u_m. Following the intermediate burst, the diffusive stage quickly sets in and mean square separation grows close to linearly. In this regime the single-scale dispersion curves normalized by $\Delta(0) l_0$ are much closer to each other, in concordance with the stated approximate linear scaling with initial separation.

The above results show that in this type of steady two-dimensional flow, superquadratic local growth of mean square separation can arise from persistent strain even in the absence of multiple flow scales. While the addition of smaller scales naturally enhances relative dispersion, it actually reduces the apparent dispersion exponent in the intermediate regime, since the separations induced by the smaller scales are not significantly increased by the large scale. In other words, a Richardson-like dispersion process across scales does not seem possible in this type of flow without the inclusion of time dependence or three-dimensional effects. Therefore, if the flows studied here are not fundamentally dissimilar from those of Rossi *et al.*,[5,6] the intermediate separation exponents measured in the experiment may also be due to practically decoupled, severe straining at the different scales. This explanation would be consistent with the increase in the separation exponent with higher forcing intensity, since the relative influence of the smaller scales diminishes as inertial forces become stronger.

VI. CONCLUSION

We have studied the spectral and particle dispersion properties of a class of steady multiscale flows similar to the electromagnetically controlled thin-layer flows of Rossi *et al.*[5–7] The forcing setups considered extend the experimental ones by allowing for different types of self-similarity as well as scaling of the forcing intensity. In this way, they facilitate assessing the influence of the scaling and geometrical parameters on the fundamental characteristics of the flows.

We have based our investigations on computations of a two-dimensional layer-averaged model, which we have justified by analogy with the behavior in the thin-layer limit. When the forcing is weak and the fluid layer is very thin, the horizontal velocity is nearly proportional to the incompressible component of the forcing and varies vertically according to a semiparabolic profile. We have numerically solved the model using a semi-Lagrangian spline code. By simulating one of the laboratory flows, we have shown that our model and numerical method reproduce the main flow features at relatively weak forcing.

Like in the experiment, the Eulerian wavenumber spectra of our theoretical flows oscillate around power laws over the wavenumber range corresponding to the forcing scales. Making use of the approximate proportionality between the forcing and the fluid velocity, we have explained the exponents of these power laws in terms of the parameters of the forcing. There is qualitative agreement between the predicted and observed exponents except at the small scales, where inertial and viscous horizontal forces are more important and proportionality fails. The obtained scaling is specific to the selected self-similar forcing, though it does not depend on the particular form of the largest forcing scale.

The Lagrangian frequency spectra show power laws as well, though preceded by low-frequency plateaus. Again using elementary similarity arguments for this type of flow and forcing, we have related the exponents of these power laws to the scaling and geometrical parameters. In this case, because of the overlapping of the velocities associated with the different scales, the predictions deteriorate as the relative intensity of the smaller scales is decreased. We have also found that the low-frequency plateaus arise from the slow motions far away from the applied forces.

The absolute dispersion of particles carried by the flows follows the Taylor phenomenology, with mean square displacement initially growing ballistically and at some point diffusively. The transition between these two well-known regimes happens near the Lagrangian correlation time, which we have found to be close to the characteristic time of the largest scale. Given that almost all particle trajectories are periodic in these steady planar flows, the decay of correlation and the presence of a diffusive regime are somewhat surprising. These two features appear because the particle ensemble spans infinitely many streamlines with incommensurate periods. However, we have not investigated the relation of these properties with shear or other characteristics of the multiscale flows.

The relative dispersion of tracer particles also presents ballistic and diffusive stages. Between these two regimes, the shape of the mean square separation curves depends on the forcing parameters and is not generally a power law. By closely inspecting both the multiscale and single-scale cases, we have verified that the intermediate regime is dominated by a succession of exponential-like separation bursts originating from the intense strain regions imposed by the different forcing scales. While these bursts can cause locally superquadratic mean square separation, the trapping action of steady recirculating regions at each scale precludes the appearance of a well-defined relative dispersion power law.

In summary, we have qualitatively explained the spectral and particle dispersion characteristics of steady multiscale thin-layer flows using plain similarity arguments. Although our analysis and results assume weak forcing, the insight gained applies also to moderately forced flows. Thus, we have been able to interpret experimental results using the same framework. It is remarkable that some Lagrangian properties yield to such simple analysis, which depends crucially on the steadiness of the flows. We intend to carry out a parallel study of time-dependent multiscale two-dimensional flows focusing on relative dispersion, connections between Eulerian and Lagrangian statistics and the role of sweeping.

ACKNOWLEDGMENTS

We gratefully acknowledge financial support from EPSRC-GB Grant No. EP/E00847X/1.

APPENDIX: COMPUTATIONAL METHOD

We solve the layer-averaged model (9) using a code initially developed for two-dimensional turbulence that combines semi-Lagrangian advection with exponential time differencing. We represent the vorticity and the streamfunction in terms of the uniform periodic B-spline basis $(\tilde{B}_i^{\kappa})_{i=1}^{n}$ of order κ and maximum regularity:[20,21]

$$\omega(x_1,x_2) = \sum_{j_1,j_2=1}^{n} \tilde{\omega}_{j_1,j_2} \tilde{B}_{j_1}^{\kappa}(x_1) \tilde{B}_{j_2}^{\kappa}(x_2), \tag{A1a}$$

$$\psi(x_1,x_2) = \sum_{j_1,j_2=1}^{n} \tilde{\psi}_{j_1,j_2} \tilde{B}_{j_1}^{\kappa}(x_1) \tilde{B}_{j_2}^{\kappa}(x_2). \tag{A1b}$$

By Eq. (9b), the velocity components are then given by

$$u_1(x_1,x_2) = \sum_{j_1,j_2=1}^{n} \tilde{\psi}_{j_1,j_2} \tilde{B}_{j_1}^{\kappa}(x_1) \tilde{B}_{j_2}^{\kappa'}(x_2), \tag{A2a}$$

$$u_2(x_1,x_2) = -\sum_{j_1,j_2=1}^{n} \tilde{\psi}_{j_1,j_2} \tilde{B}_{j_1}^{\kappa'}(x_1) \tilde{B}_{j_2}^{\kappa}(x_2). \tag{A2b}$$

The B-coefficients $\tilde{\omega}_{j_1,j_2}$ and $\tilde{\psi}_{j_1,j_2}$ are determined by the values of the fields at the points of the form (ξ_{i_1},ξ_{i_2}), with $(\xi_i)_{i=1}^{n}$ being the interior knot averages of the B-splines.

We discretize the Poisson equation (9b) by collocation at the knot averages, and thus obtain the linear system

$$\sum_{j_1,j_2=1}^{n} \tilde{\psi}_{j_1,j_2}[\tilde{B}_{j_1}^{\kappa''}(\xi_{i_1})\tilde{B}_{j_2}^{\kappa}(\xi_{i_2}) + \tilde{B}_{j_1}^{\kappa}(\xi_{i_1})\tilde{B}_{j_2}^{\kappa''}(\xi_{i_2})]$$

$$= -\sum_{j_1,j_2=1}^{n} \tilde{\omega}_{j_1,j_2}\tilde{B}_{j_1}^{\kappa}(\xi_{i_1})\tilde{B}_{j_2}^{\kappa}(\xi_{i_2}), \tag{A3}$$

which we solve using the discrete Fourier transform.

We discretize the linear part of the model (9a) analogously and obtain the system of evolution equations

$$\sum_{j_1,j_2=1}^{n} \left[\frac{d\tilde{\omega}_{j_1,j_2}}{dt} + \frac{3}{2}(\beta\tilde{\omega}_{j_1,j_2} - \tilde{\varphi}_{j_1,j_2})\right]\tilde{B}_{j_1}^{\kappa}(\xi_{i_1})\tilde{B}_{j_2}^{\kappa}(\xi_{i_2})$$

$$= \sum_{j_1,j_2=1}^{n} \nu\tilde{\omega}_{j_1,j_2}[\tilde{B}_{j_1}^{\kappa''}(\xi_{i_1})\tilde{B}_{j_2}^{\kappa}(\xi_{i_2}) + \tilde{B}_{j_1}^{\kappa}(\xi_{i_1})\tilde{B}_{j_2}^{\kappa''}(\xi_{i_2})], \tag{A4}$$

where $\tilde{\varphi}_{j_1,j_2}$ are the B-coefficients of the vorticity forcing. We numerically integrate these evolution equations using a second-order exponential time differencing method.[22]

The advective part of Eq. (9) is simply the transport of vorticity by a scaled velocity. Thus, in a semi-Lagrangian advective step, the final vorticity at a given collocation point $\boldsymbol{\xi}$ should equal the initial vorticity at the departure point $\boldsymbol{\Xi}$ that reaches $\boldsymbol{\xi}$ by the end of the time step.[23] Knowing the solution at time t, we first calculate first-order estimates for the departure points given by

$$\boldsymbol{\Xi}^{*} = \boldsymbol{\xi} - \tfrac{4}{5}\Delta t\mathbf{u}(\boldsymbol{\xi},t). \tag{A5}$$

We then compute a first-order approximation to the vorticity at time $t+\Delta t$ in the form

$$\omega^{*}(\boldsymbol{\xi}) = \omega(\boldsymbol{\Xi}^{*},t), \tag{A6}$$

which in turn yields a first-order approximation $\mathbf{u}^{*}$ to the velocity at time $t+\Delta t$. A second-order estimate for the departure points is then given by

$$\boldsymbol{\Xi}^{**} = \boldsymbol{\xi} - \tfrac{2}{5}\Delta t\left[\mathbf{u}^{*}(\boldsymbol{\xi}) + \mathbf{u}\left(\boldsymbol{\xi} - \tfrac{4}{5}\Delta t\mathbf{u}^{*}(\boldsymbol{\xi}),t\right)\right]. \tag{A7}$$

These points lead to the following second-order estimate for the vorticity at time $t+\Delta t$:

$$\omega^{**}(\boldsymbol{\xi}) = \omega(\boldsymbol{\Xi}^{**},t), \tag{A8}$$

which completes the semi-Lagrangian advective step.

We blend the methods for the advective and linear parts of the model using the second-order symmetric splitting of Strang.[24] At each time step, we first evolve the vorticity according to the viscous and forcing terms for half a time step. We subsequently advect the vorticity for one time step and lastly repeat the linear half-step.

[1] P. A. Davidson, *Turbulence: An Introduction for Scientists and Engineers* (Oxford University Press, Oxford, 2004).
[2] P. Constantin and I. Procaccia, "Scaling in fluid turbulence: A geometric theory," Phys. Rev. E **47**, 3307 (1993).
[3] J. Davila and J. C. Vassilicos, "Richardson's pair diffusion and the stagnation point structure of turbulence," Phys. Rev. Lett. **91**, 144501 (2003).
[4] S. Goto and J. C. Vassilicos, "Particle pair diffusion and persistent streamline topology in two-dimensional turbulence," New J. Phys. **6**, 65 (2004).
[5] L. Rossi, J. C. Vassilicos, and Y. Hardalupas, "Electromagnetically controlled multi-scale flows," J. Fluid Mech. **558**, 207 (2006).
[6] L. Rossi, J. C. Vassilicos, and Y. Hardalupas, "Multiscale laminar flows with turbulentlike properties," Phys. Rev. Lett. **97**, 144501 (2006).
[7] L. Rossi, J. C. Vassilicos, and Y. Hardalupas, "Eulerian-Lagrangian aspects of a steady multiscale laminar flow," Phys. Fluids **19**, 078108 (2007).
[8] B. Juttner, D. Marteau, P. Tabeling, and A. Thess, "Numerical simulations of experiments on quasi-two-dimensional turbulence," Phys. Rev. E **55**, 5479 (1997).
[9] M. P. Satijn, A. W. Cense, R. Verzicco, H. J. H. Clercx, and G. J. F. van Heijst, "Three-dimensional structure and decay properties of vortices in shallow fluid layers," Phys. Fluids **13**, 1932 (2001).
[10] E. Hascoët, L. Rossi, and J. C. Vassilicos, in *IUTAM Symposium on Flow Control and MEMS*, edited by J. F. Morrison, D. M. Birch, and P. Lavoie (Springer, New York, 2008).
[11] R. A. D. Akkermans, A. R. Cieslik, L. P. J. Kamp, R. R. Trieling, H. J. H. Clercx, and G. J. F. van Heijst, "The three-dimensional structure of an electromagnetically generated dipolar vortex in a shallow fluid layer," Phys. Fluids **20**, 116601 (2008).
[12] S. Lardeau, S. Ferrari, and L. Rossi, "Three-dimensional direct numerical simulation of electromagnetically driven multiscale shallow layer flows: Numerical modeling and physical properties," Phys. Fluids **20**, 127101 (2008).
[13] P. A. Davidson, *An Introduction to Magnetohydrodynamics* (Cambridge University Press, Cambridge, 2001).
[14] V. G. Levich, *Physicochemical Hydrodynamics* (Prentice-Hall, Englewood Cliffs, NJ, 1962).
[15] G. D. Fulford, "Flow of liquids in thin films," Adv. Chem. Eng. **5**, 151 (1964).
[16] S. A. Nazarov, "Asymptotic solution of the Navier–Stokes problem on the flow of a thin-layer of fluid," Sib. Math. J. **31**, 296 (1990).
[17] K. Toraichi, M. Kamada, S. Itahashi, and R. Mori, "Window functions represented by B-spline functions," IEEE Trans. Acoust., Speech, Signal Process. **37**, 145 (1989).
[18] H. Tennekes and J. L. Lumley, *A First Course in Turbulence* (MIT Press, Cambridge, MA, 1972).
[19] P. G. Saffman, *Vortex Dynamics* (Cambridge University Press, Cambridge, 1992).
[20] C. de Boor, *A Practical Guide to Splines* (Springer, New York, 1978).
[21] O. Botella and K. Shariff, "B-spline methods in fluid dynamics," Int. J. Comput. Fluid Dyn. **17**, 133 (2003).
[22] S. M. Cox and P. C. Matthews, "Exponential time differencing for stiff systems," J. Comput. Phys. **176**, 430 (2002).
[23] A. Staniforth and J. Cote, "Semi-Lagrangian integration schemes for atmospheric models—A review," Mon. Weather Rev. **119**, 2206 (1991).
[24] G. Strang, "On the construction and comparison of difference schemes," SIAM (Soc. Ind. Appl. Math.) J. Numer. Anal. **5**, 506 (1968).